COMPDYN 2011
3rd ECCOMAS Thematic Conference on
Computational Methods in Structural Dynamics and Earthquake Engineering
M. Papadrakakis, M. Fragiadakis, V. Plevris (eds.)
Corfu, Greece, 25–28 May 2011

NONLINEAR MODAL ANALYSIS OF AEROSPACE STRUCTURES

M. Peeters[1], G. Kerschen[1], J.C. Golinval[1], C. Stephan[2], and P. Lubrina[2]

[1]Aerospace and Mechanical Engineering Department
University of Lige, Lige, Belgium
e-mail: g.kerschen@ulg.ac.be

[2] Office National dEtudes et de Recherches Aerospatiales (ONERA), DADS-ADSE
Chatillon, France

Keywords: Modal Analysis, Nonlinearity, Aerospace.

Abstract. *The dynamic systems theory is well-established for linear systems and can rely on mature tools such as the theories of linear operators and linear integral transforms. This is why theoretical and experimental modal analysis, i.e., the computation of vibration modes from a mathematical model and from experimental data, respectively, is really quite sophisticated and advanced. Even though linear modal analysis served, and is still serving, the structural dynamics community for applications ranging from bridges to satellites, it is commonly accepted that nonlinearity is a frequent occurrence in engineering structures.*

Because linear modal analysis fails in the presence of nonlinear dynamical phenomena, the development of a practical nonlinear analog of modal analysis would be an extremely timely contribution; it is clearly missing in the structural dynamics literature. A new framework for nonlinear modal analysis of real-world structures, which includes the computation of nonlinear modes from finite element models, is introduced in this paper. This framework will permit a rigorous, yet understandable by the practicing engineer, analysis of nonlinear dynamical phenomena. It will also provide solid theoretical foundations for extending finite element model validation to nonlinear aerospace structures.

1 INTRODUCTION

Nonlinear normal modes (NNMs) offer a solid theoretical and mathematical tool for interpreting a wide class of nonlinear dynamical phenomena, yet they have a clear and simple conceptual relation to the LNMs [1, 2, 3]. However, most structural engineers still view NNMs as a concept that is foreign to them, and they do not yet consider NNMs as a useful concept for structural dynamics. One reason supporting this statement is that most existing constructive techniques for computing NNMs are based on asymptotic approaches and rely on fairly involved mathematical developments.

There have been very few attempts to compute NNMs using numerical methods [4, 5, 6, 7]. Algorithms for the continuation of periodic solutions are really quite sophisticated and advanced (see, e.g., [8, 9, 10]), and they have been extensively used for computing the forced response and limit cycles of nonlinear dynamical systems (see, e.g., [11]). Interestingly, they have not been fully exploited for the computation of nonlinear modes.

In this paper, we support that these numerical algorithms pave the way for an effective and practical computation of NNMs. The proposed algorithm, implemented in MATLAB, relies on two main techniques, namely a shooting procedure and a method for the continuation of NNM motions. The objective is to demonstrate that the numerical computation of the NNMs of complex real-world structures is then within reach. The application considered in this study is the airframe of the Morane-Saulnier Paris aircraft, whose ground vibration tests have exhibited some nonlinear structural behaviors.

2 Nonlinear Normal Modes (NNMs)

A detailed description of NNMs and their fundamental properties (e.g., frequency-energy dependence, bifurcations and stability) is given in [1, 2, 3]. For completeness, the two main definitions of an NNM are briefly reviewed in this section.

The free response of discrete conservative mechanical systems with n degrees of freedom (DOFs) is considered, assuming that continuous systems (e.g., beams, shells or plates) have been spatially discretized using the finite element method. The equations of motion are

$$\mathbf{M}\,\ddot{\mathbf{x}}(t) + \mathbf{K}\,\mathbf{x}(t) + \mathbf{f}_{\text{nl}}\left\{\mathbf{x}(t), \dot{\mathbf{x}}(t)\right\} = 0 \tag{1}$$

where $\mathbf{M}$ is the mass matrix; $\mathbf{K}$ is the stiffness matrix; $\mathbf{x}$, $\dot{\mathbf{x}}$ and $\ddot{\mathbf{x}}$ are the displacement, velocity and acceleration vectors, respectively; $\mathbf{f}_{\text{nl}}$ is the nonlinear restoring force vector.

There exist two main definitions of an NNM in the literature due to Rosenberg and Shaw and Pierre:

1. Targeting a straightforward nonlinear extension of the linear normal mode (LNM) concept, Rosenberg defined an NNM motion as a *vibration in unison* of the system (i.e., a synchronous periodic oscillation).

2. To provide an extension of the NNM concept to damped systems, Shaw and Pierre defined an NNM as a two-dimensional invariant manifold in phase space. Such a manifold is invariant under the flow (i.e., orbits that start out in the manifold remain in it for all time), which generalizes the invariance property of LNMs to nonlinear systems.

At first glance, Rosenberg's definition may appear restrictive in two cases. Firstly, it cannot be easily extended to nonconservative systems. However, the damped dynamics can often be interpreted based on the topological structure of the NNMs of the underlying conservative

system [3]. Secondly, in the presence of internal resonances, the NNM motion is no longer synchronous, but it is still periodic.

In the present study, an NNM motion is therefore defined as a *(non-necessarily synchronous) periodic motion* of the conservative mechanical system (1). As we will show, this extended definition is particularly attractive when targeting a numerical computation of the NNMs. It enables the nonlinear modes to be effectively computed using algorithms for the continuation of periodic solutions.

3 Numerical Computation of NNMs

The numerical method proposed here for the NNM computation relies on two main techniques, namely a shooting technique and the pseudo-arclength continuation method. A detailed description of the algorithm is given in [12].

3.1 Shooting Method

The equations of motion of system (1) can be recast into state space form

$$\dot{\mathbf{z}} = \mathbf{g}(\mathbf{z}) \tag{2}$$

where $\mathbf{z} = \begin{bmatrix}\mathbf{x}^* & \dot{\mathbf{x}}^*\end{bmatrix}^*$ is the $2n$-dimensional state vector, and star denotes the transpose operation, and

$$\mathbf{g}(\mathbf{z}) = \begin{pmatrix} \dot{\mathbf{x}} \\ -\mathbf{M}^{-1}\left[\mathbf{K}\mathbf{x} + \mathbf{f}_{\text{nl}}(\mathbf{x}, \dot{\mathbf{x}})\right] \end{pmatrix} \tag{3}$$

is the vector field. The solution of this dynamical system for initial conditions $\mathbf{z}(0) = \mathbf{z}_0 = \begin{bmatrix}\mathbf{x}_0^* & \dot{\mathbf{x}}_0^*\end{bmatrix}^*$ is written as $\mathbf{z}(t) = \mathbf{z}\left(t, \mathbf{z}_0\right)$ in order to exhibit the dependence on the initial conditions, $\mathbf{z}\left(0, \mathbf{z}_0\right) = \mathbf{z}_0$. A solution $\mathbf{z}_p(t, \mathbf{z}_{p0})$ is a periodic solution of the autonomous system (2) if $\mathbf{z}_p(t, \mathbf{z}_{p0}) = \mathbf{z}_p(t + T, \mathbf{z}_{p0})$, where T is the minimal period.

The NNM computation is carried out by finding the periodic solutions of the governing nonlinear equations of motion (2). In this context, the *shooting method* is probably the most popular numerical technique. It solves numerically the two-point boundary-value problem defined by the periodicity condition

$$\mathbf{H}(\mathbf{z}_{p0}, T) \equiv \mathbf{z}_p(T, \mathbf{z}_{p0}) - \mathbf{z}_{p0} = \mathbf{0} \tag{4}$$

$\mathbf{H}(\mathbf{z}_0, T) = \mathbf{z}(T, \mathbf{z}_0) - \mathbf{z}_0$ is called the *shooting function* and represents the difference between the initial conditions and the system response at time T. Unlike forced motion, the period T of the free response is not known a priori.

The shooting method consists in finding, in an iterative way, the initial conditions $\mathbf{z}_{p0}$ and the period T that realize a periodic motion. To this end, the method relies on direct numerical time integration and on the Newton-Raphson algorithm.

Starting from some assumed initial conditions $\mathbf{z}_{p0}^{(0)}$, the motion $\mathbf{z}_p^{(0)}(t, \mathbf{z}_{p0}^{(0)})$ at the assumed period $T^{(0)}$ can be obtained by numerical time integration methods (e.g., Runge-Kutta or Newmark schemes). In general, the initial guess $(\mathbf{z}_{p0}^{(0)}, T^{(0)})$ does not satisfy the periodicity condition (4). A Newton-Raphson iteration scheme is therefore to be used to correct an initial guess and to converge to the actual solution. The corrections $\Delta\mathbf{z}_{p0}^{(k)}$ and $\Delta T^{(k)}$ at iteration k are found by expanding the nonlinear function

$$\mathbf{H}\left(\mathbf{z}_{p0}^{(k)} + \Delta\mathbf{z}_{p0}^{(k)}, T^{(k)} + \Delta T^{(k)}\right) = 0 \tag{5}$$

in Taylor series and neglecting higher-order terms (H.O.T.).

The phase of the periodic solutions is not fixed. If $\mathbf{z}(t)$ is a solution of the autonomous system (2), then $\mathbf{z}(t+\Delta t)$ is geometrically the same solution in state space for any Δt. Hence, an additional condition, termed the *phase condition*, has to be specified in order to remove the arbitrariness of the initial conditions. This is discussed in detail in [12].

In summary, an isolated NNM is computed by solving the augmented two-point boundary-value problem defined by

$$\mathbf{F}(\mathbf{z}_{p0}, T) \equiv \left\{ \begin{array}{rcl} \mathbf{H}(\mathbf{z}_{p0}, T) & = & 0 \\ h(\mathbf{z}_{p0}) & = & 0 \end{array} \right. \tag{6}$$

where $h(\mathbf{z}_{p0}) = 0$ is the phase condition.

3.2 Continuation of Periodic Solutions

Due to the frequency-energy dependence, the modal parameters of an NNM vary with the total energy. An NNM family, governed by equations (6), therefore traces a curve, termed an NNM branch, in the $(2n+1)$-dimensional space of initial conditions and period $(\mathbf{z}_{p0}, T)$. Starting from the corresponding LNM at low energy, the computation is carried out by finding successive points $(\mathbf{z}_{p0}, T)$ of the NNM branch using methods for the *numerical continuation* of periodic motions (also called *path-following methods*) [8, 9]. The space $(\mathbf{z}_{p0}, T)$ is termed the continuation space.

Different methods for numerical continuation have been proposed in the literature. The so-called pseudo-arclength continuation method is used herein.

Starting from a known solution $(\mathbf{z}_{p0,(j)}, T_{(j)})$, the next periodic solution $(\mathbf{z}_{p0,(j+1)}, T_{(j+1)})$ on the branch is computed using a *predictor step* and a *corrector step*.

Predictor step

At step j, a prediction $(\tilde{\mathbf{z}}_{p0,(j+1)}, \tilde{T}_{(j+1)})$ of the next solution $(\mathbf{z}_{p0,(j+1)}, T_{(j+1)})$ is generated along the tangent vector to the branch at the current point $\mathbf{z}_{p0,(j)}$

$$\left[\begin{array}{c} \tilde{\mathbf{z}}_{p0,(j+1)} \\ \tilde{T}_{(j+1)} \end{array} \right] = \left[\begin{array}{c} \mathbf{z}_{p0,(j)} \\ T_{(j)} \end{array} \right] + s_{(j)} \left[\begin{array}{c} \mathbf{p}_{z,(j)} \\ p_{T,(j)} \end{array} \right] \tag{7}$$

where $s_{(j)}$ is the predictor stepsize. The tangent vector $\mathbf{p}_{(j)} = [\mathbf{p}_{z,(j)}^* \; p_{T,(j)}]^*$ to the branch defined by (6) is solution of the system

$$\left[\begin{array}{cc} \left.\frac{\partial \mathbf{H}}{\partial \mathbf{z}_{p0}}\right|_{(\mathbf{z}_{p0,(j)}, T_{(j)})} & \left.\frac{\partial \mathbf{H}}{\partial T}\right|_{(\mathbf{z}_{p0,(j)}, T_{(j)})} \\ \left.\frac{\partial h}{\partial \mathbf{z}_{p0}}^*\right|_{(\mathbf{z}_{p0,(j)})} & 0 \end{array} \right] \left[\begin{array}{c} \mathbf{p}_{z,(j)} \\ p_{T,(j)} \end{array} \right] = \left[\begin{array}{c} \mathbf{0} \\ 0 \end{array} \right] \tag{8}$$

with the condition $\left\|\mathbf{p}_{(j)}\right\| = 1$. The star denotes the transpose operator. This normalization can be taken into account by fixing one component of the tangent vector and solving the resulting overdetermined system using the Moore-Penrose matrix inverse; the tangent vector is then normalized to 1.

Corrector step

The prediction is corrected by a shooting procedure in order to solve (6) in which the variations of the initial conditions and the period are forced to be orthogonal to the predictor step. At iteration k, the corrections

$$\begin{aligned} \mathbf{z}_{p0,(j+1)}^{(k+1)} &= \mathbf{z}_{p0,(j+1)}^{(k)} + \Delta\mathbf{z}_{p0,(j+1)}^{(k)} \\ T_{(j+1)}^{(k+1)} &= T_{(j+1)}^{(k)} + \Delta T_{(j+1)}^{(k)} \end{aligned} \tag{9}$$

are computed by solving the overdetermined linear system using the Moore-Penrose matrix inverse

$$\begin{bmatrix} \frac{\partial \mathbf{H}}{\partial \mathbf{z}_{p0}}\Big|_{(\mathbf{z}_{p0,(j+1)}^{(k)}, T_{(j+1)}^{(k)})} & \frac{\partial \mathbf{H}}{\partial T}\Big|_{(\mathbf{z}_{p0,(j+1)}^{(k)}, T_{(j+1)}^{(k)})} \\ \frac{\partial h}{\partial \mathbf{z}_{p0}}^{*}\Big|_{(\mathbf{z}_{p0,(j+1)}^{(k)})} & 0 \\ \mathbf{p}_{z,(j)}^{*} & p_{T,(j)} \end{bmatrix} \begin{bmatrix} \Delta\mathbf{z}_{p0,(j+1)}^{(k)} \\ \Delta T_{(j+1)}^{(k)} \end{bmatrix} = \begin{bmatrix} -\mathbf{H}(\mathbf{z}_{p0,(j+1)}^{(k)}, T_{(j+1)}^{(k)}) \\ -h(\mathbf{z}_{p0,(j+1)}^{(k)}) \\ 0 \end{bmatrix} \tag{10}$$

where the prediction is used as initial guess, i.e, $\mathbf{z}_{p0,(j+1)}^{(0)} = \tilde{\mathbf{z}}_{p0,(j+1)}$ and $T_{(j+1)}^{(0)} = \tilde{T}_{(j+1)}$. The last equation in (10) corresponds to the orthogonality condition for the corrector step.

This iterative process is carried out until convergence is achieved. The convergence test is based on the relative error of the periodicity condition:

$$\frac{\|\mathbf{H}(\mathbf{z}_{p0}, T)\|}{\|\mathbf{z}_{p0}\|} = \frac{\|\mathbf{z}_p(T, \mathbf{z}_{p0}) - \mathbf{z}_{p0}\|}{\|\mathbf{z}_{p0}\|} < \epsilon \tag{11}$$

where ϵ is the prescribed relative precision.

3.3 Sensitivity Analysis

Each shooting iteration involves the time integration of the equations of motion to evaluate the current shooting residue $\mathbf{H}\left(\mathbf{z}_{p0}^{(k)}, T^{(k)}\right) = \mathbf{z}_p^{(k)}(T^{(k)}, \mathbf{z}_{p0}^{(k)}) - \mathbf{z}_{p0}^{(k)}$. As evidenced by equation (10), the method also requires the evaluation of the $2n \times 2n$ Jacobian matrix

$$\frac{\partial \mathbf{H}}{\partial \mathbf{z}_0}(\mathbf{z}_0, T) = \left.\frac{\partial \mathbf{z}(t, \mathbf{z}_0)}{\partial \mathbf{z}_0}\right|_{t=T} - \mathbf{I} \tag{12}$$

where $\mathbf{I}$ is the $2n \times 2n$ identity matrix.

The classical finite-difference approach requires to perturb successively each of the $2n$ initial conditions and integrate the *nonlinear* governing equations of motion. This approximate method therefore relies on extensive numerical simulations and may be computationally intensive for large-scale finite element models.

Targeting a reduction of the computational cost, a significant improvement is to use sensitivity analysis for determining $\partial\mathbf{z}(t, \mathbf{z}_0)/\partial\mathbf{z}_0$ instead of a numerical finite-difference procedure. The sensitivity analysis consists in differentiating the equations of motion (2) with respect to the initial conditions $\mathbf{z}_0$ which leads to

$$\frac{d}{dt}\left[\frac{\partial \mathbf{z}(t, \mathbf{z}_0)}{\partial \mathbf{z}_0}\right] = \left.\frac{\partial \mathbf{g}(\mathbf{z})}{\partial \mathbf{z}}\right|_{\mathbf{z}(t,\mathbf{z}_0)} \left[\frac{\partial \mathbf{z}(t, \mathbf{z}_0)}{\partial \mathbf{z}_0}\right] \tag{13}$$

with

$$\frac{\partial \mathbf{z}(0, \mathbf{z}_0)}{\partial \mathbf{z}_0} = \mathbf{I} \tag{14}$$

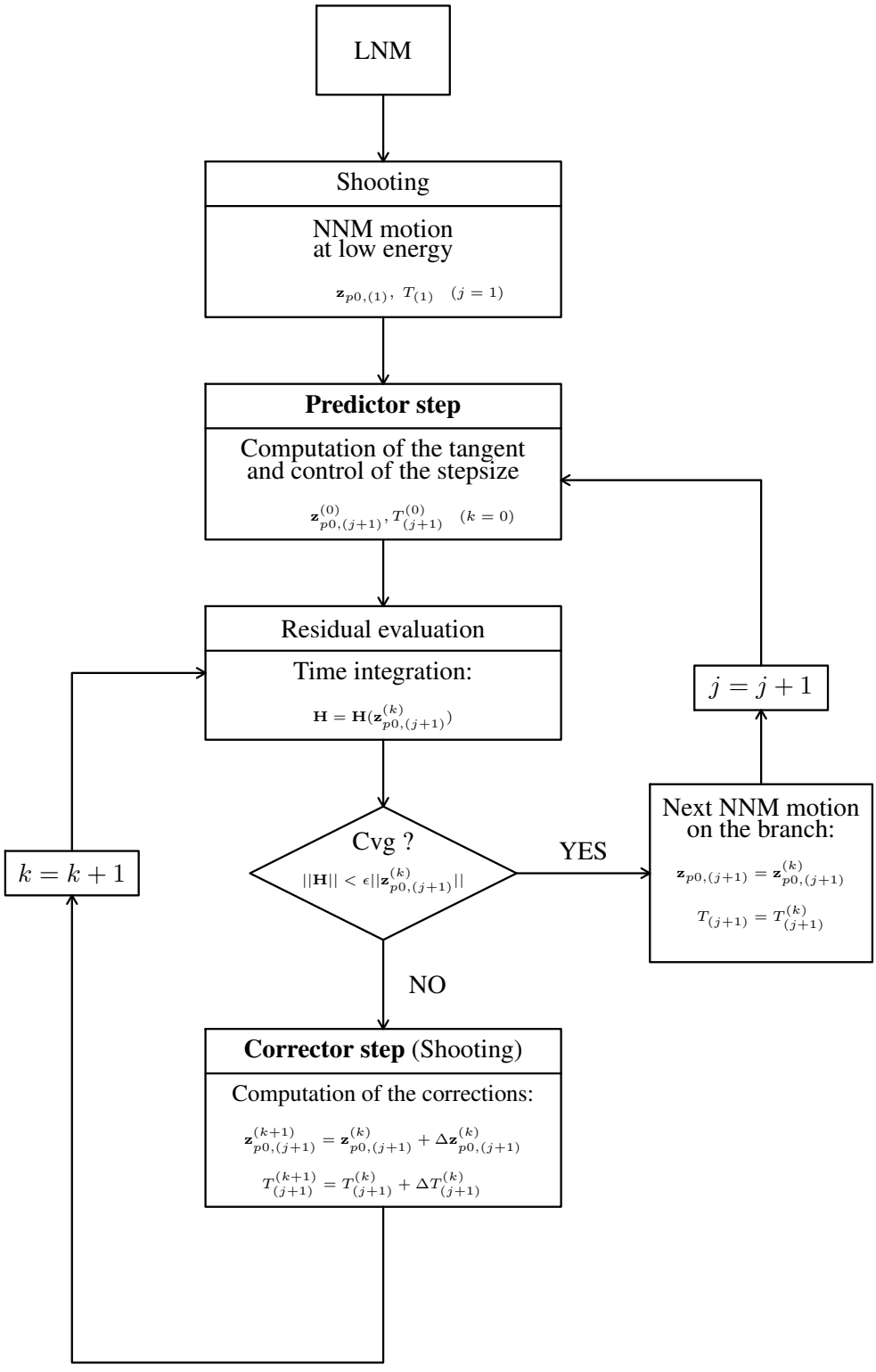

Figure 1: Algorithm for NNM computation.

since $\mathbf{z}(0, \mathbf{z}_0) = \mathbf{z}_0$. Hence, the matrix $\partial \mathbf{z}(t, \mathbf{z}_0)/\partial \mathbf{z}_0$ at $t = T$ can be obtained by numerically integrating over T the initial-value problem defined by the *linear* ordinary differential equations (ODEs) (13) with the initial conditions (14).

In addition to the integration of the current solution $\mathbf{z}(t, \mathbf{x}_0)$ of (2), these two methods for computing $\partial \mathbf{z}(t, \mathbf{z}_0)/\partial \mathbf{z}_0$ require $2n$ numerical integrations of $2n$-dimensional dynamical systems, which may be computationally intensive for large systems. However, equations (13) are linear ODEs and their numerical integration is thus less expensive. The numerical cost can be further reduced if the solution of equations (13) is computed together with the solution of the nonlinear equations of motion in a single numerical simulation [13].

The sensitivity analysis requires only one additional iteration at each time step of the numerical time integration of the current motion to provide the Jacobian matrix. The reduction of the computational cost is therefore significant for large-scale finite element models. In addition, the Jacobian computation by means of the sensitivity analysis is exact. The convergence troubles regarding the chosen perturbations of the finite-difference method are then avoided. Hence, the use of sensitivity analysis to perform the shooting procedure represents a meaningful improvement from a computational point of view.

As the monodromy matrix $\partial \mathbf{z}_p(T, \mathbf{z}_{p0})/\partial \mathbf{z}_{p0}$ is computed, its eigenvalues, the Floquet multipliers, are obtained as a by-product, and the stability analysis of the NNM motions can be performed in a straightforward manner.

3.4 Algorithm for NNM Computation

The algorithm proposed for the computation of NNM motions is a combination of shooting and pseudo-arclength continuation methods, as shown in Figure 1. It has been implemented in the MATLAB environment. Other features of the algorithm such as the step control, the reduction of the computational burden and the method used for numerical integration of the equations of motion are discussed in [12].

So far, the NNMs have been considered as branches in the continuation space $(\mathbf{z}_{p0}, T)$. An appropriate graphical depiction of the NNMs is to represent them in a frequency-energy plot (FEP). This FEP can be computed in a straightforward manner: (i) the conserved total energy is computed from the initial conditions realizing the NNM motion; and (ii) the frequency of the NNM motion is calculated directly from the period.

4 Numerical Experiment - Full-Scale Aircraft

The numerical computation of the NNMs of a complex real-world structure is addressed. This structure is the airframe of the Morane-Saulnier Paris aircraft, which is represented in Figure 2. This French jet aircraft was built during the 1950s and was used as a trainer and liaison aircraft. The structural configuration under consideration corresponds to the aircraft without its jet engines and standing on the ground through its three landing gears with deflated tires. For information, general characteristics are listed in Table 1. A specimen of this plane is present in ONERA's laboratory, and ground vibration tests have exhibited nonlinear behavior in the connection between the wings and external fuel tanks located at the wing tip. As illustrated in Figure 3, this connection consists of bolted attachments.

Figure 2: Morane-Saulnier Paris aircraft.

Table 1: Properties of the Morane-Saulnier Paris aircraft

Length (m)	Wingspan (m)	Height (m)	Wing area (m^2)	Weight (kg)
10.4	10.1	2.6	18	1945

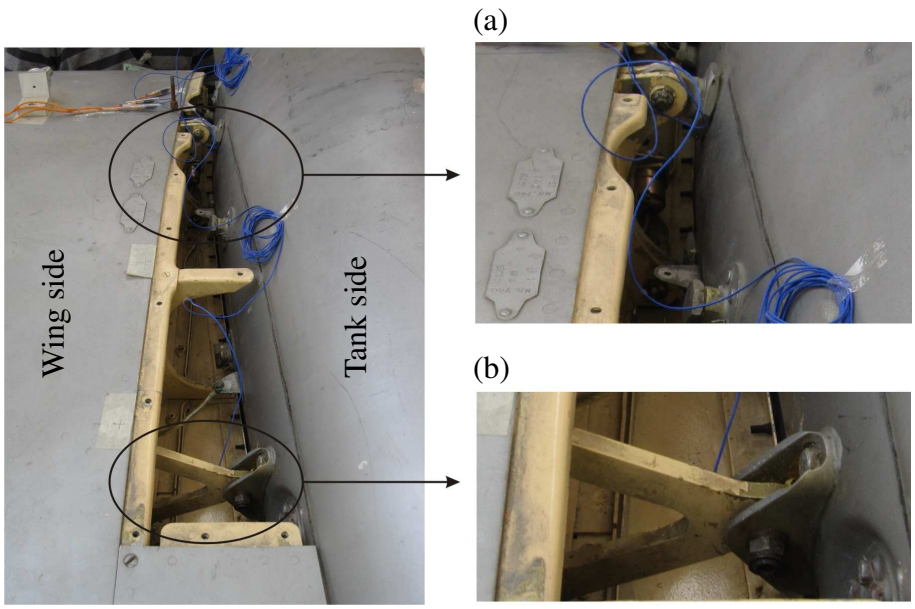

Figure 3: Connection between external fuel tank and wing tip (top view). Close-up of (a) front and (b) rear bolted attachments.

4.1 Structural Model of the Paris Aircraft

4.1.1 Finite Element Model of the Underlying Linear Structure

The linear finite element model of the full-scale aircraft, illustrated in Figure 4, was elaborated from drawings by ONERA [14]. The wings, vertical stabilizer, horizontal tail and fuselage are modeled by means of 2-dimensional elements such as beams and shells. The complete finite element model has more than 80000 DOFs. Three-dimensional spring elements, which take into account the structural flexibility of the tires and landing gears, are used as boundary conditions of the aircraft. At each wing tip, the external fuel tank is connected with front and rear attachments (see Figure 3). In this linear model, these connections between the wings and the fuel tanks are modeled using beam elements. The linear model, originally created in the Nastran software, was converted and exploited in the Samcef finite element environment for this study.

The natural frequencies of the underlying linear system in the [0-50Hz] frequency range are given in Table 2. The first nine modes correspond to aircraft rigid-body modes: six modes are modes of suspensions of the landing gear while the three others are associated to rigid-body motions of the control surfaces (i.e., the ailerons, elevator and rudder). The frequency range of the rigid-body modes is comprised between 0.09 and 3.57 Hz, i.e., noticeably lower than the first flexible mode located at 8.19 Hz. The modal shapes of different elastic normal modes of vibrations are depicted in Figure 5. Figure 5(a) represents the first wing bending mode. The first and second wing torsional modes are depicted in Figures 5(b) and 5(c). These two torsional modes correspond to symmetric and anti-symmetric wing motions, respectively. As shown thereafter, these modes are of particular interest in nonlinear regime since there is a significant deformation of the connections between the wings and fuel tanks. Indeed, the other modes mainly concern the aircraft tail and are consequently almost unaffected by these nonlinear connections.

4.1.2 Reduced-Order Model

The proposed algorithm for the numerical computation of NNMs is computationally intensive for the large-scale original model possessing more than 80000 DOFs. Since the nonlinearities are spatially localized, condensation of the linear components of the model is an appealing approach for a computationally tractable and efficient calculation.

A reduced-order model of the linear finite element system is constructed using the Craig-Bampton (also called component mode) reduction technique [15]. This method consists in describing the system in terms of some retained DOFs and internal vibration modes. By partitioning the complete system in terms of n_R remaining $\mathbf{x}_R$ and $n_C = n - n_R$ condensed $\mathbf{x}_C$ DOFs, the n governing equations of motion of the global finite element model are written as

$$\begin{bmatrix} \mathbf{M}_{RR} & \mathbf{M}_{RC} \\ \mathbf{M}_{CR} & \mathbf{M}_{CC} \end{bmatrix} \begin{bmatrix} \ddot{\mathbf{x}}_R \\ \ddot{\mathbf{x}}_C \end{bmatrix} + \begin{bmatrix} \mathbf{K}_{RR} & \mathbf{K}_{RC} \\ \mathbf{K}_{CR} & \mathbf{K}_{CC} \end{bmatrix} \begin{bmatrix} \mathbf{x}_R \\ \mathbf{x}_C \end{bmatrix} = \begin{bmatrix} \mathbf{g}_R \\ \mathbf{0} \end{bmatrix} \tag{15}$$

The Craig-Bampton method expresses the complete set of initial DOFs in terms of: (i) the remaining DOFs through the static modes (resulting from unit displacements on the remaining DOFs) and (ii) a certain number $m < n_C$ of internal vibration modes (relating to the primary structure fixed on the remaining nodes). Mathematically, the reduction is described by relation

$$\begin{bmatrix} \mathbf{x}_R \\ \mathbf{x}_C \end{bmatrix} = \begin{bmatrix} \mathbf{I} & \mathbf{0} \\ -\mathbf{K}_{CC}^{-1}\mathbf{K}_{CR} & \mathbf{\Phi}_m \end{bmatrix} \begin{bmatrix} \mathbf{x}_R \\ \mathbf{y} \end{bmatrix} = \mathbf{R} \begin{bmatrix} \mathbf{x}_R \\ \mathbf{y} \end{bmatrix} \tag{16}$$

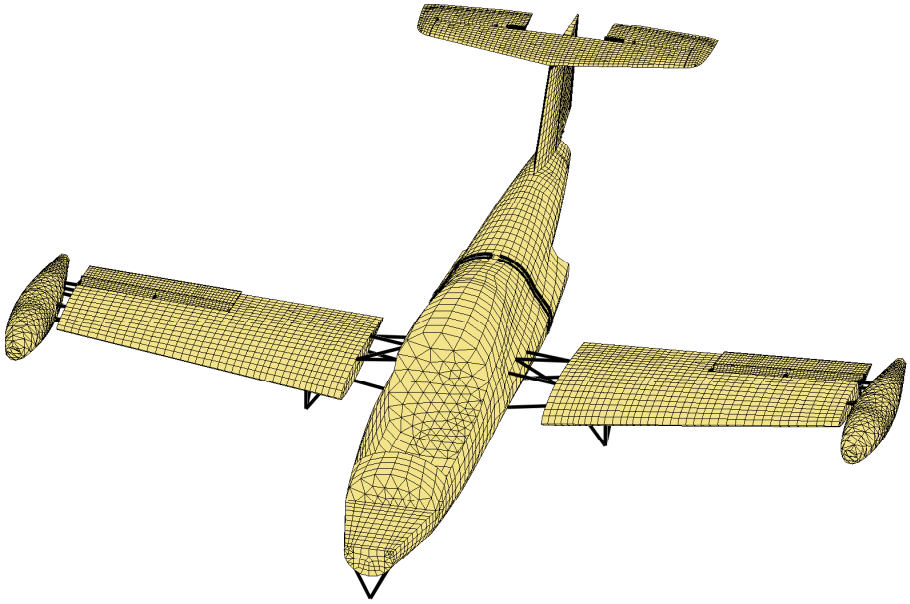

Figure 4: Finite element model of the Morane-Saulnier Paris aircraft.

Mode	Freq. (Hz)	Mode	Freq. (Hz)
1	0.0936	13	21.2193
2	0.7260	14	22.7619
3	0.9606	15	23.6525
4	1.2118	16	25.8667
5	1.2153	17	28.2679
6	1.7951	18	29.3309
7	2.1072	19	31.0847
8	2.5157	20	34.9151
9	3.5736	21	39.5169
10	8.1913	22	40.8516
11	9.8644	23	47.3547
12	16.1790	24	52.1404

Table 2: Natural frequencies of the linear finite element model of the Paris aircraft.

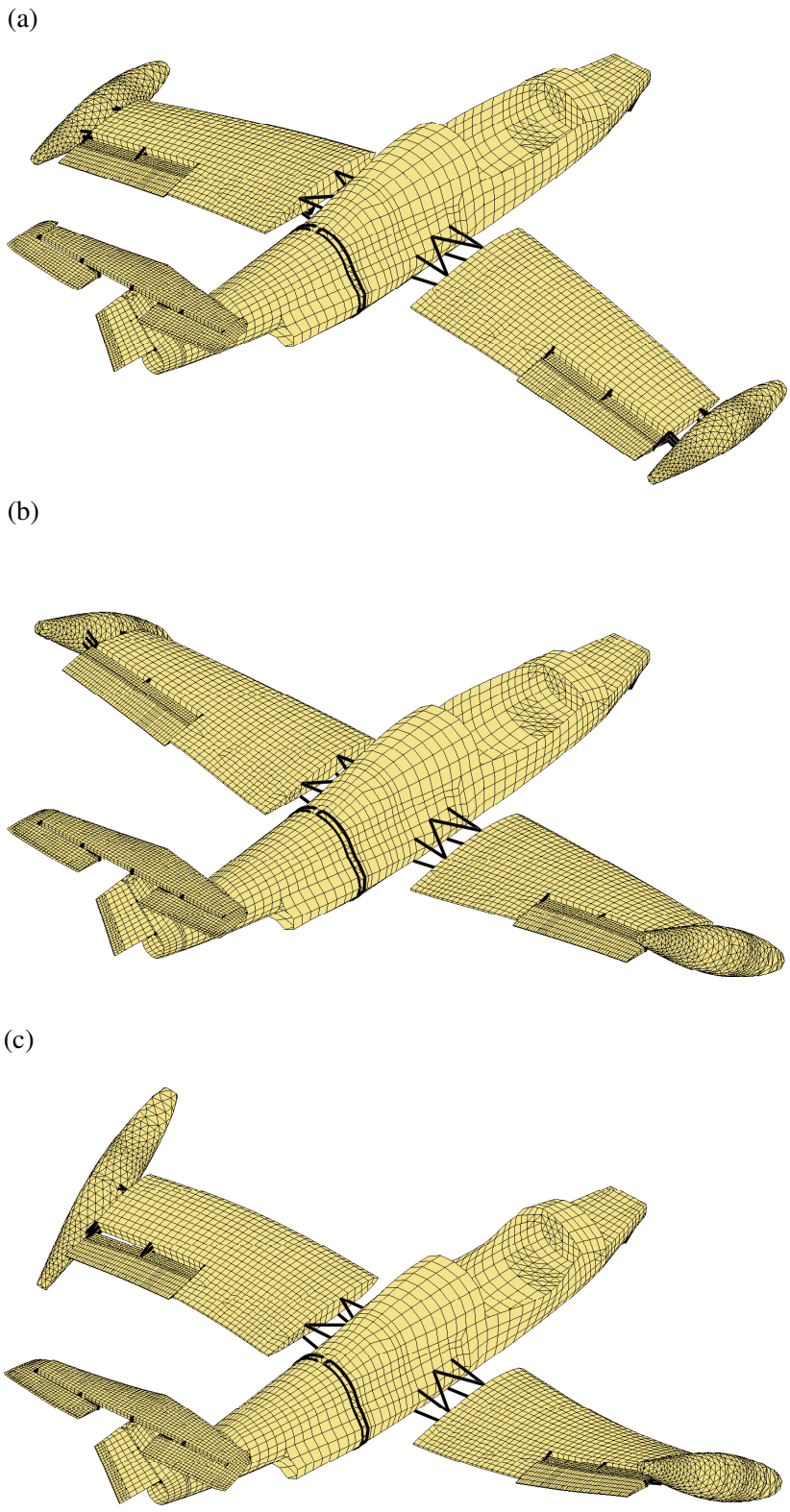

Figure 5: Normal modes of the linear finite element model of the Morane-Saulnier Paris aircraft. (a) First wing bending mode (8.19 Hz), (b) first (symmetric) wing torsional mode (31.08 Hz) and (b) second (anti-symmetric) wing torsional mode (34.92 Hz).

which defines the $n \times (n_R + m)$ reduction matrix $\mathbf{R}$. $\mathbf{y}$ are the modal coordinates of the m internal linear normal modes collected in the $n_C \times m$ matrix $\mathbf{\Phi}_m = [\phi_{(1)} \dots \phi_{(m)}]$. These modes are solutions of the linear eigenvalue problem corresponding to the system fixed on the remaining nodes

$$\left(\mathbf{K}_{CC} - \omega_{(j)}^2 \mathbf{M}_{CC}\right) \phi_{(j)} = \mathbf{0} \tag{17}$$

The reduced model is thus defined by the $(n_R + m) \times (n_R + m)$ reduced stiffness and mass matrices given by

$$\begin{aligned} \overline{\mathbf{M}} &= \mathbf{R}^* \mathbf{M} \mathbf{R} \\ \overline{\mathbf{K}} &= \mathbf{R}^* \mathbf{K} \mathbf{R} \end{aligned} \tag{18}$$

where star denotes the transpose operation. After reduction, the system configuration is expressed in terms of the reduced coordinates (i.e., the remaining DOFs and the modal coordinates). The initial DOFs of the complete model are then determined by means of the reduction matrix using relation 16.

In order to introduce the nonlinear behavior of the connections between the wings and the tanks, the reduced-order linear model of the aircraft is constructed by keeping one node on both sides of the attachments. For each wing, four nodes are retained: two nodes for the front attachment and two nodes for the rear attachment. In total, only eight nodes of the finite element model are kept to build the reduced model. It is completed by holding the first 500 internal modes of vibrations. Finally, the model is thus reduced to 548 DOFs: 6 DOFs per node (3 translations and 3 rotations) and 1 DOF per internal mode. The reduction is performed using the Samcef software. The generated reduced-order model is next exported in the MATLAB environment.

Before proceeding to nonlinear analysis, the accuracy of the reduced-order linear model is assessed. To this end, the linear normal modes of the initial complete finite element model are compared to those predicted by the reduced model. The deviation between the mode shapes of the original model $\mathbf{x}_{(o)}$ and of the reduced model $\mathbf{x}_{(r)}$ is determined using the Modal Assurance Criterion (MAC)

$$\text{MAC} = \frac{\left|\mathbf{x}_{(o)}^* \mathbf{x}_{(r)}\right|^2}{\left|\mathbf{x}_{(o)}^* \mathbf{x}_{(o)}\right| \left|\mathbf{x}_{(r)}^* \mathbf{x}_{(r)}\right|} \tag{19}$$

MAC values range from 0 in case of no correlation to 1 for a complete coincidence. In the [0-100Hz] range, MAC values between modes shapes are all greater than 0.999 and the maximum relative error on the natural frequencies is 0.2%. It therefore validates the excellent accuracy of the reduced linear model in this frequency range. It is worth noticing that less internal modes are sufficient to ensure such as a correlation in the [0-100Hz] frequency range, which is typically the range of interest for aircrafts. However, a larger number of modes was deliberately chosen for two main reasons. On the one side, it serves to illustrate the ability of the numerical algorithm to deal with the NNM computation of higher-dimensional systems. On the other hand, due to nonlinearity, modes of higher frequencies may interact with lower modes of interest. In nonlinear regimes, higher internal modes should then be necessary to guarantee the accuracy of the model.

Figure 6: Instrumentation of the rear attachment of the right wing.

4.1.3 Nonlinear Model

The existence of a softening nonlinear behavior was evidenced during different vibration tests conducted by ONERA. In particular, FRF measurements reveal the decrease of resonant frequencies with the level of excitation. The connections between the wings and fuel tanks are assumed to cause this observed nonlinear effect.

To confirm this hypothesis, both (front and rear) connections of each wing were instrumented and experimental measurements were carried out. Specifically, accelerometers were positioned on both (wing and tank) sides of the connections and two shakers were located at the tanks. This is illustrated in Figure 6 for rear connection.

The dynamic behavior of these connections in the vertical direction is investigated using the restoring force surface (RFS) method [16]. By writing Newton's second law at the wing side of each connection, it follows

$$m_c \ddot{x}_c(t) + f_{r,c} = 0 \tag{20}$$

where $f_{r,c}$ is the restoring force applied to this point. The index c is related to the connection under consideration (i.e., either the rear or front attachment of the left or right wing). From Equation (20), the restoring force is obtained by

$$f_{r,c} = -m_c \ddot{x}_c(t) \tag{21}$$

Except the multiplicative mass factor m_c, the restoring force is then given by the acceleration $\ddot{x}_c(t)$. Nevertheless, this total restoring force does not consist only of the internal force related to the connection of interest, but also includes contributions from the linking forces associated to the wing elastic deformation. Provided that these latter do not play a prominent role, the measurement of the acceleration signal may still provide a qualitative insight into the nonlinear part of the restoring force in the connection between the tank and the wing.

The aircraft is excited close to the second torsional mode (see Figure 5(c)) using a band-limited swept sine excitation in the vicinity of its corresponding resonant frequency. In Figure 7, the measured acceleration at the wing side is represented in terms of the relative displacement x_{rel} and velocity $\dot{x}_{rel}$ of the connection obtained by integrating the accelerations on both sides of the attachment. It is given for the rear connections of the right and left wings. A nonlinear softening elastic effect is observed from the evolution of these estimated restoring force surfaces. In particular, the detected behavior has a piecewise characteristic. This is more clearly

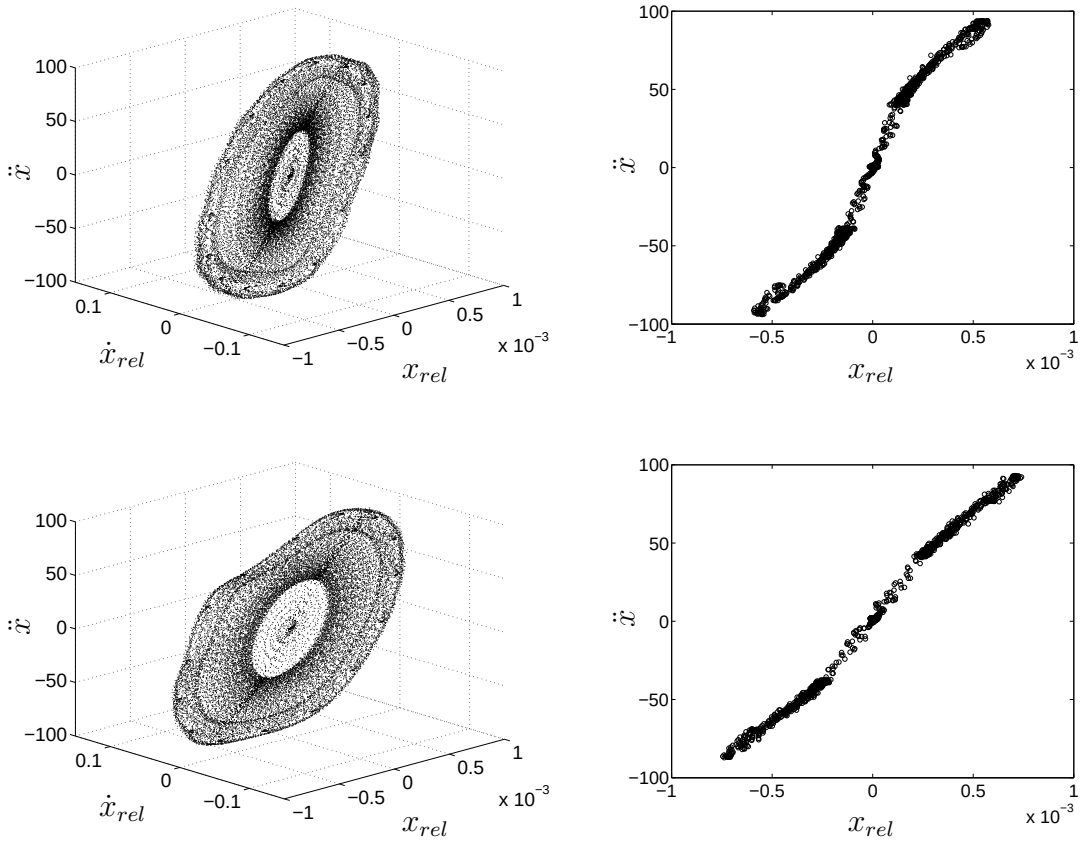

Figure 7: Estimated restoring force in the connections between tanks and wings. Left plots: measured acceleration in terms of the relative displacement (m) and velocity (m/s). Right plots: stiffness curve given by the measured acceleration for zero velocity. Top plots: rear tank connection of the left wing. Bottom plots: rear tank connection of the right wing.

evidenced by the corresponding stiffness curves also depicted in Figure 7. Softening nonlinearity is typical of bolted connections [17, 18]. Similar nonlinear effect occurs for the front connections, but they participate much less in the considered response. Finally, the deviation between the right and left connections seems to show asymmetry of the connections.

Although purely qualitative, the RFS results therefore indicate that the tank connections present a softening stiffness in the vertical direction. As previously mentioned, a model with piecewise characteristic might be consistent with the experimental observations. However, the NNM algorithm, in its present form, cannot handle nonsmooth nonlinearities. Alternatively, linear and negative cubic stiffness terms are one possible manner of describing the observed nonlinear behavior. Indeed, the reconstructed stiffness curve obtained by fitting to the data the mathematical model

$$f_{r,c} = kx_{rel} + k_{nl}^{-} x_{rel}^{3} \qquad (k_{nl}^{-} < 0) \tag{22}$$

is in relatively good agreement.

In view of the qualitative value of this approach, we note that the objective followed here is to derive a simplified realistic model in order to illustrate the numerical computation procedure of NNMs. Accordingly, in the present study, the nonlinear behavior is modeled by adding negative cubic stiffness nonlinearities into the linear part of the connections. An indicative value of -10^{13}N/m^3 is adopted for each connection. Finally, the nonlinear system is then constructed from the reduced-order model by means of cubic springs positioned vertically between both corresponding nodes retained on either side of connections.

4.2 Nonlinear Normal Modes

From the nonlinear reduced-order model, the numerical computation of NNMs is realized in the MATLAB environment using the previously developed algorithm. The goal followed here is to show that the proposed method can deal with complex structures such as this real-aircraft model. In this context, this section focuses on some specific modes.

4.2.1 Fundamental NNMs

The modes of the aircraft can be classified into two categories, depending on whether they correspond to wing motions or not. The modes localized mainly on other structural parts (such as the vertical stabilizer, the horizontal tail or the fuselage) are almost unaffected by the nonlinear connections located at the wing tips. Only the modes involving wing deformations are perceptibly affected by nonlinearity. According to the relative motion of the fuel tanks, these modes are more or less altered for increasing energy levels.

An unaffected mode is first examined in Figure 8. It corresponds to the nonlinear extension of the first tail bending LNM (mode 13 in Table 2). In this figure, the computed backbone and related NNM motions are depicted in the FEP. The modal shapes are given in terms of the initial displacements (with zero initial velocities assumed) that realize the NNM motion. It clearly confirms that the modal shape and the oscillation frequency remain practically unchanged with the energy in the system.

Modes involving wing deformations are now investigated. The first wing bending mode (i.e., the nonlinear extension of mode 10 in Table 2) is illustrated in Figure 9. The FEP reveals that this mode is weakly affected by the nonlinearities. The frequency of the NNM motions on the backbone slightly decreases with increasing energy levels, which results from the softening characteristic of the nonlinearity. Regarding the modal shapes, they are almost similar over the

energy range and resemble the corresponding LNM. MAC value between the NNM shapes at low and high energy levels (see (a) and (b) in Figure 9) is 0.99.

Figure 10 represents the FEP of the first (symmetric) wing torsional mode (i.e., mode 19 in Table 2). For this mode, the relative motion of the fuel tanks is more important, which enhances the nonlinear effect of the connections. As a result, the oscillation frequency have a more marked energy dependence along the backbone branch. On the other hand, the modal shapes are still weakly altered. MAC value between the NNM shapes on the backbone at low and high energy levels (see (a) and (b) in Figure 10) is equal to 0.98. In addition, the FEP highlights the presence of three tongues, revealing the existence of internal resonances between this symmetric torsional mode and other modes. These observed modal interactions are discussed in the next section.

Finally, the second (anti-symmetric) wing torsional mode (i.e., mode 20 in Table 2) is plotted in the FEP of Figure 11. While the oscillation frequency is noticeably altered by nonlinearity, modal shapes are again slightly changed. Over the energy range of interest, the decrease in frequency is around 5% along the backbone branch. MAC value between the modal shapes at low and high energy levels (see (a) and (b) in Figure 11) is 0.97. It shows that the nonlinearities spatially localized between the wing tips and the tanks weakly influence the NNM spatial shapes. Besides the NNM backbone, one tongue is present at higher energy. For information, the computation of the backbone branch up to the tongue needs 20 min with 100 time steps over the half period (using Intel i7 920 2.67GHz processor). Due to the presence of turning points, the computation of the tongue is more expensive and demands about one hour.

Similar dynamics were observed for the higher modes and are not further described herein.

4.2.2 Internally Resonant NNMs

Besides the backbone branches, the previous FEPs show the presence of tongues of internally resonant NNMs. Following a resonance scenario similar to that described in [3], theses additional branches emanate from the backbone of a specific NNM and coalesce into the backbone branch of another NNM, thereby realizing an internal resonance between the two modes.

This is briefly illustrated in Figure 12 regarding the 3:1 tongue emanating from the backbone of the first wing torsional mode (see Figure 10). Modal shapes are given at three different locations on the tongue (see (a), (b) and (c) in Figure 12). When the energy gradually increases along the tongue, a smooth transition from the first wing torsional mode to a higher tail torsional mode clearly occurs. Interestingly, Figure 12(b) shows an inherently nonlinear mode with no counterpart in the underlying linear system. It corresponds to a 3:1 internal resonance as evidenced by the evolution of the time series and the frequency content, also represented in Figure 12, of the periodic motions along the tongue. A third harmonic progressively appears, and the structure vibrates according to a subharmonic motion characterized by two dominant frequency components. The relative importance of the third harmonic grows along the tongue, until the mode transition is realized.

Similarly, two other tongues corresponding to a 5:1 and a 9:1 internal resonance between this first wing torsional mode and higher modes are observed in the FEP of Figure 10. Moreover, the FEP of Figure 11 reveals the presence of a 9:1 internal resonance between the second wing torsional mode and another higher mode of the aircraft. We note that the practical realization of these internal resonances is questionable in view of the low frequency changes.

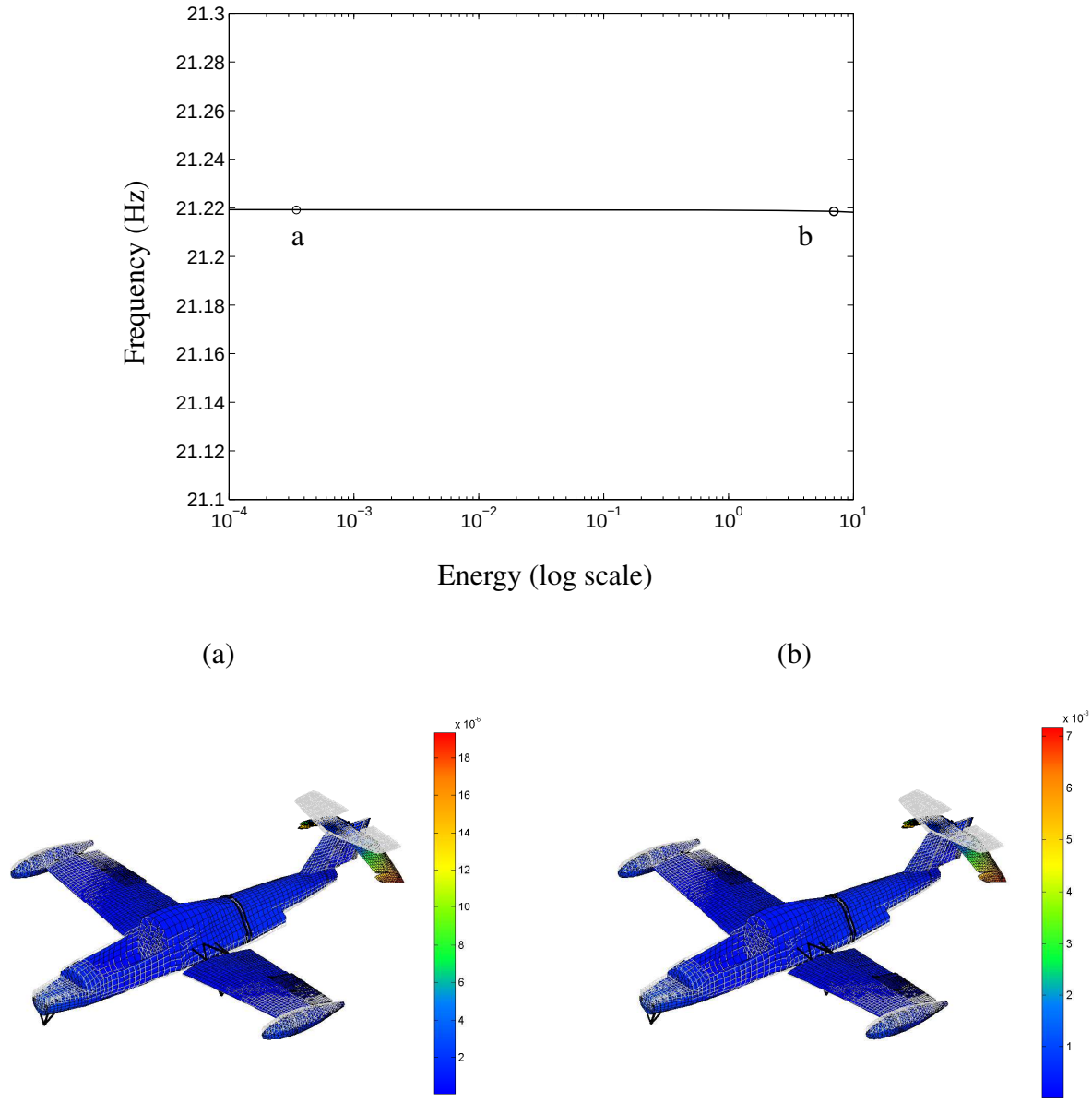

Figure 8: FEP of the first tail bending NNM of the Paris aircaft. NNM shapes at energy levels marked in the FEP are inset; they are given in terms of the initial displacements (m) that realize the periodic motion (with zero initial velocities assumed).

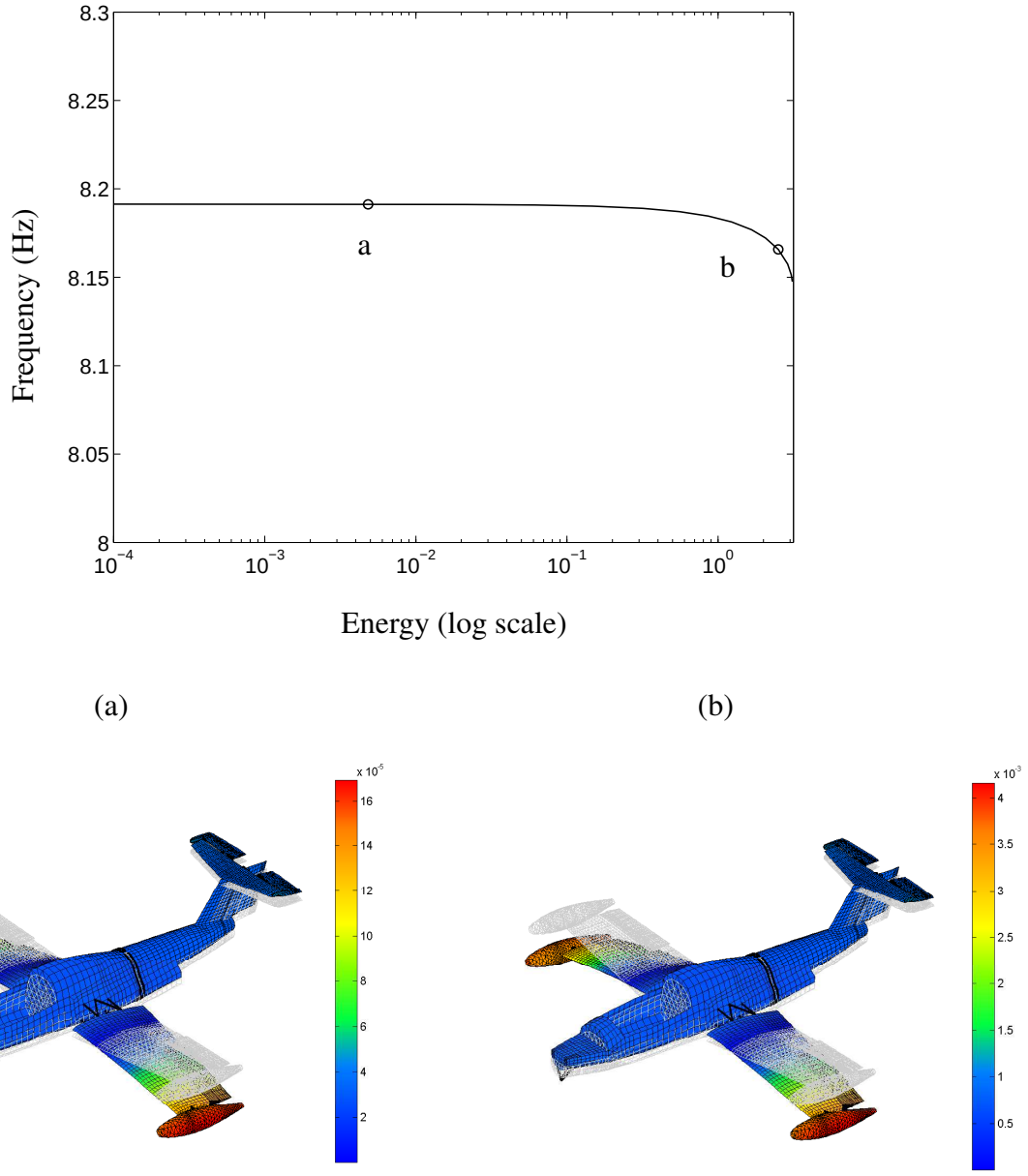

Figure 9: FEP of the first wing bending NNM of the Paris aircraft. NNM shapes at energy levels marked in the FEP are inset; they are given in terms of the initial displacements (m) that realize the periodic motion (with zero initial velocities assumed).

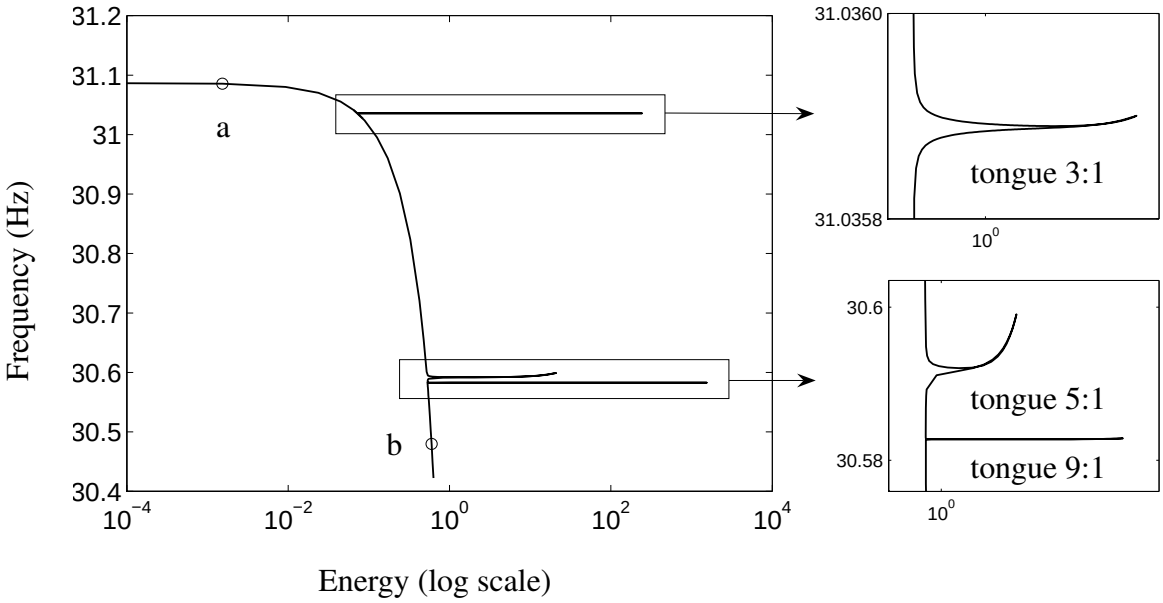

Figure 10: FEP of the first (symmetric) wing torsional NNM of the Paris aircraft. NNM shapes at energy levels marked in the FEP are inset; they are given in terms of the initial displacements (m) that realize the periodic motion (with zero initial velocities assumed).

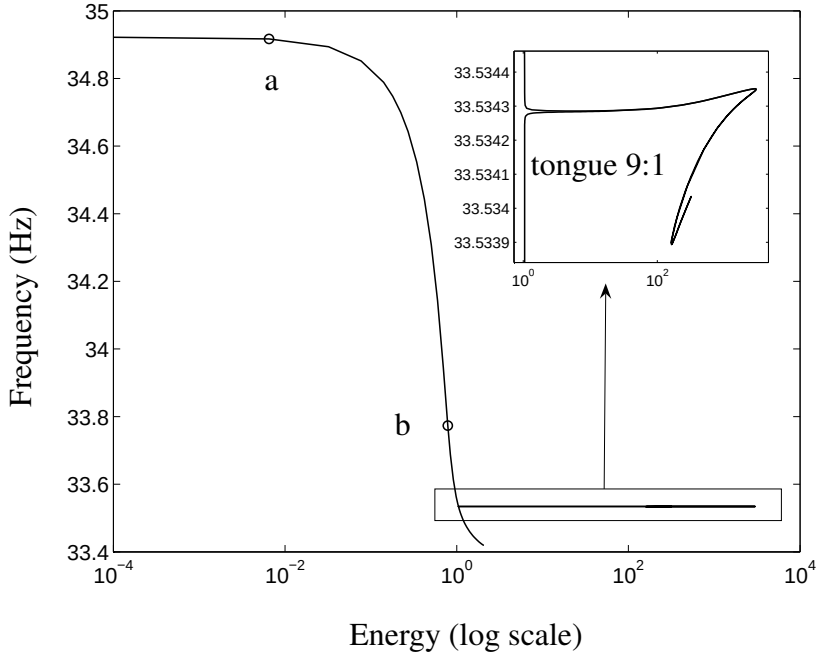

Figure 11: FEP of the second (anti-symmetric) wing torsional NNM of the Paris aircraft. NNM shapes at energy levels marked in the FEP are inset; they are given in terms of the initial displacements (m) that realize the periodic motion (with zero initial velocities assumed).

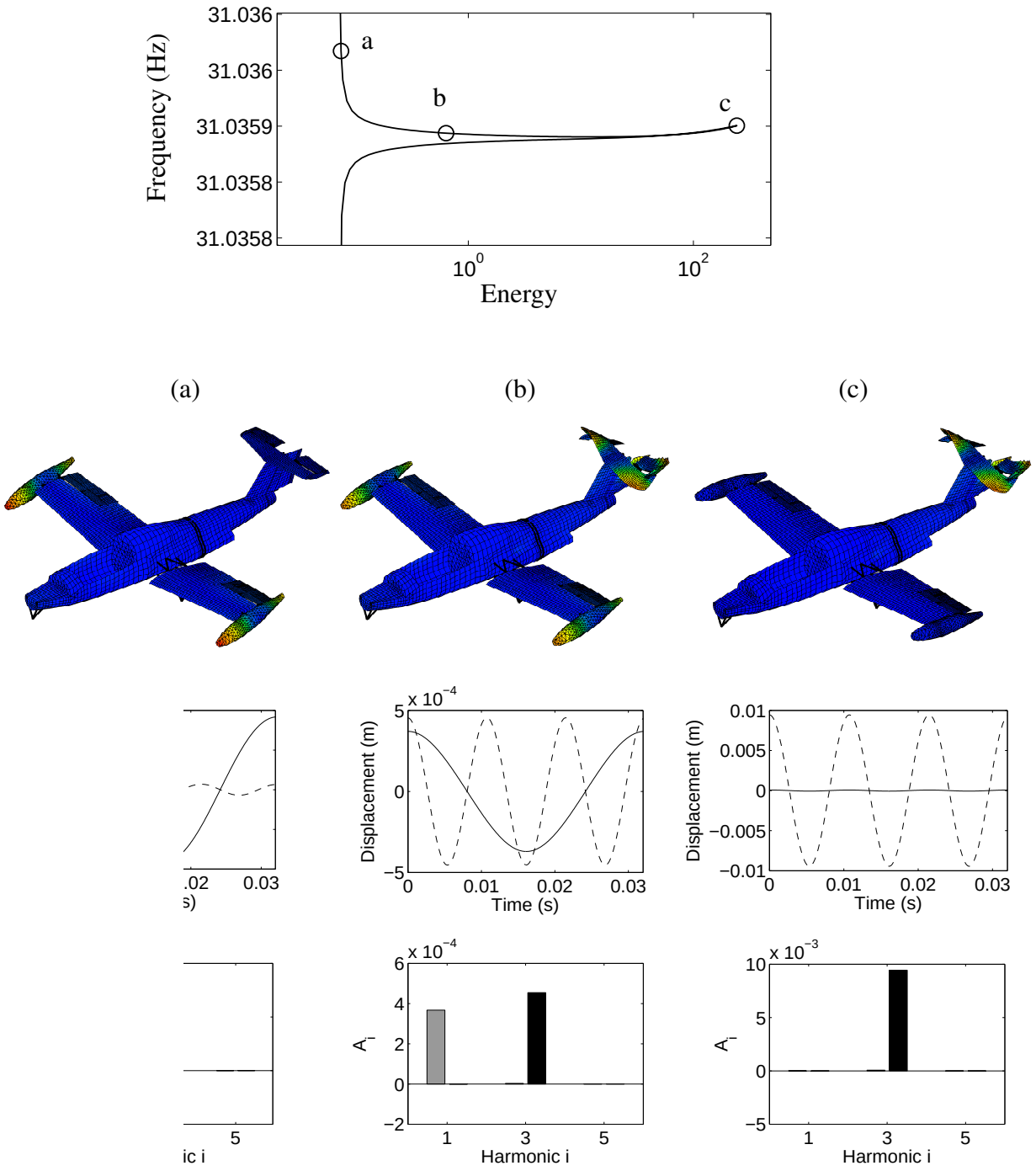

Figure 12: 3:1 internal resonance between the first wing torsional mode and a higher tail mode of the Paris aircraft. Top plot: close-up in the FEP of the 3:1 tongue of Figure 10. Bottom plots: NNM motions at (a) beginning of the tongue (in the vicinity of the backbone of the the first wing torsional mode); (b) middle of the tongue; and (c) extremity of the tongue. From top to bottom: NNM shapes; time series of the vertical displacements at the rear tip of the right tank (——) and at the right side of the horizontal tail (– – –); Fourier coefficients of both displacements (in grey and black, respectively).

5 Conclusion

In this paper, a numerical method for the computation of NNMs of mechanical structures was introduced. The approach targets the computation of the undamped modes of structures discretized by finite elements and relies on the continuation of periodic solutions.

This computational approach turns out to be capable of dealing with complex real-world structures, such as the full-scale aircraft studied herein. Through a reduced-order model accurate in the [0-100Hz] range, the NNMs were indeed computed accurately even in strongly nonlinear regimes and with a reasonable computational burden. Internal resonances were also computed by the algorithm and were briefly discussed.

REFERENCES

[1] A.F. Vakakis, L.I. Manevitch, Y.V. Mikhlin, V.N. Pilipchuk, A.A. Zevin, *Normal Modes and Localization in Nonlinear Systems*, John Wiley & Sons, New York (1996).

[2] A.F. Vakakis, *Non-linear normal modes (NNMs) and their applications in vibration theory: An overview*, Mechanical Systems and Signal Processing, Vol. 11, No. 1 (1997), pp. 3-22.

[3] G. Kerschen, M. Peeters, J.C. Golinval, A.F. Vakakis, *Nonlinear normal modes, Part I: A useful framework for the structural dynamicist*, Mechanical Systems and Signal Processing, Vol. 23, No. 1 (2009), pp. 170-194.

[4] J.C. Slater, *A numerical method for determining nonlinear normal modes*, Nonlinear Dynamics, Vol. 10, No. 1 (1996), pp. 19-30.

[5] E. Pesheck, *Reduced-order modeling of nonlinear structural systems using nonlinear normal modes and invariant manifolds*, PhD Thesis, University of Michigan, Ann Arbor (2000).

[6] Y.S. Lee, G. Kerschen, A.F. Vakakis, P.N. Panagopoulos, L.A. Bergman, D.M. McFarland, *Complicated dynamics of a linear oscillator with a light, essentially nonlinear attachment*, Physica D-Nonlinear Phenomena, Vol. 204, No. 1-2 (2005), pp. 41-69.

[7] R. Arquier, S. Bellizzi, R. Bouc, B. Cochelin, *Two methods for the computation of nonlinear modes of vibrating systems at large amplitudes*, Computers & Structures, Vol. 84, No. 24-25 (2006), pp. 1565-1576.

[8] R. Seydel, *Practical Bifurcation and Stability Analysis, from Equilibirum to Chaos*, Springer-Verlag, 2nd Edition (1994).

[9] A.H. Nayfeh, B. Balachandran, *Applied Nonlinear Dynamics: Analytical, Computational, and Experimental Methods*, Wiley-Interscience, New York (1995).

[10] E. Doedel, *AUTO, Software for Continuation and Bifurcation Problems in Ordinary Differential Equations*, (2007).

[11] C. Touz, A. Amabili, O. Thomas, *Reduced-order models for large-amplitude vibrations of shells including in-plane inertia*, In *Proceedings of the EUROMECH Colloquium on Geometrically Nonlinear Vibrations, Porto, Portugal, July 2007*, Porto (2007).

[12] M. Peeters, R. Vigui, G. Srandour, G. Kerschen, J.C. Golinval, *Nonlinear normal modes, Part II: Toward a practical computation using numerical continuation techniques*, Mechanical Systems and Signal Processing, Vol. 23, No. 1 (2009), pp. 195-216.

[13] O. Brüls, P. Eberhard, *Sensitivity analysis for dynamic mechanical systems with finite rotations*, International Journal for Numerical Methods in Engineering, Vol. 1 (2006), pp. 1-29.

[14] A. Remy, *Updating of the finite element model of the MS 760 Paris aircraft*, Training period report at ONERA (2006).

[15] R. Craig, M. Bampton, *Coupling of substructures for dynamic analysis*, AIAA Journal, Vol. 6 (1968), pp. 1313–1319.

[16] S.F. Masri, T.K. Caughey, *A nonparametric identification technique for nonlinear dynamic problems*, Journal of Applied Mechanics, Vol. 46 (1979), pp. 433-447.

[17] L. Gaul, J. Lenz, *Nonlinear dynamics of structures assembled by bolted joints*, Acta Mechanica, Vol. 125 (1997), pp. 169-181.

[18] C.J. Hartwigsen, Y. Song, D.M. McFarland, L.A. Bergman, A.F. Vakakis, *Experimental study of non-linear effects in a typical shear lap joint configuration*, Journal of Sound and Vibration, Vol. 277 (2004), pp. 327-351.